PNAS RESEARCH ARTICLE | PHYSICS

Differentiated roles of Lifshitz transition on thermodynamics and superconductivity in $La_{2-x}Sr_xCuO_4$

Yong Zhong[a,b,c,d,1,2], Zhuoyu Chen[a,c,d,1,2,3], Su-Di Chen[a,c,d], Ke-Jun Xu[a,c,d], Makoto Hashimoto[e], Yu He[f], Shin-ichi Uchida[g], Donghui Lu[e], Sung-Kwan Mo[b], and Zhi-Xun Shen[a,c,d,h,2]

Contributed by Zhi-Xun Shen; received March 17, 2022; accepted June 7, 2022; reviewed by Peter Armitage and Antony Carrington

The effect of Lifshitz transition on thermodynamics and superconductivity in hole-doped cuprates has been heavily debated but remains an open question. In particular, an observed peak of electronic specific heat is proposed to originate from fluctuations of a putative quantum critical point p^* (e.g., the termination of pseudogap at zero temperature), which is close to but distinguishable from the Lifshitz transition in overdoped La-based cuprates where the Fermi surface transforms from hole-like to electron-like. Here we report an in situ angle-resolved photoemission spectroscopy study of three-dimensional Fermi surfaces in $La_{2-x}Sr_xCuO_4$ thin films ($x = 0.06$ to 0.35). With accurate k_z dispersion quantification, the said Lifshitz transition is determined to happen within a finite range around $x = 0.21$. Normal state electronic specific heat, calculated from spectroscopy-derived band parameters, reveals a doping-dependent profile with a maximum at $x = 0.21$ that agrees with previous thermodynamic microcalorimetry measurements. The account of the specific heat maximum by underlying band structures excludes the need for additionally dominant contribution from the quantum fluctuations at p^*. A *d*-wave superconducting gap smoothly across the Lifshitz transition demonstrates the insensitivity of superconductivity to the dramatic density of states enhancement.

superconductivity | photoemission | cuprates | Lifshitz transition

Significance

The existence of quantum criticality in cuprate superconductor has been an unsolved puzzle for over 3 decades. Recent thermodynamic measurements display a heat capacity peak in the vicinity of the putative quantum critical point in La-based cuprates. We systematically study the three-dimensional electronic structure of $La_{2-x}Sr_xCuO_4$ thin film in a wide doping range, to elucidate the dominant role of Lifshitz transition on the specific heat anomaly. Furthermore, a canonical *d*-wave pairing symmetry across the Lifshitz transition excludes the scenario of high-temperature superconductivity being associated with van Hove singularity.

The underlying physics of the rich phase diagram in hole-doped cuprates remains an open question (1–4). The undoped material is a Mott insulator. The nature of the Fermi surface changes as a function of doping p: for very small p it is a small pocket with no correspondence with the band theory, but it evolves into a large hole-like piece centered at (π, π) as suggested by the band calculation (5). With further increase of doping, a Lifshitz transition (LT) of the Fermi surface is expected when the chemical potential crosses the van Hove singularity (VHS), at which the Fermi surface transforms from a hole-like piece around (π, π) to an electron-like piece around (0, 0) (5, 6). On the theoretical front, the presence of VHS was suggested to be important for the enhanced T_C and phase fluctuations (6–8). Two-dimensional Hubbard model simulations proposed that this transition has a strong influence on the phase diagram of hole-doped cuprates (9–11). For certain band structure parameters, the VHS was associated with a critical point that changes the characters of superconductivity (10, 11). Recent experimental progress, including the putative termination point of pseudogap (12), the presumed quantum critical points seen in electronic specific heat and Hall number (13), and the anomalously low superfluid density in electromagnetic response in overdoped regime (14, 15), reveals unanticipated surprises in highly doped region where the LT is expected. Further, the anomaly seen in specific heat and Hall number in $La_{2-x}Sr_xCuO_4$ (LSCO) and related compounds was attributed to the quantum critical point p^* (e.g., termination of pseudogap) in a fashion that cannot be accounted for by the VHS (13, 16–19). Given the richness of experimental phenomenology and theoretical postulations, a systematic study of the electronic structure across the LT is desirable.

Angle-resolved photoemission spectroscopy (ARPES) is a powerful tool to visualize Fermi surface in momentum space (20), yielding quantitative agreements with the results from quantum oscillation experiments (21–24). LTs have been explored in different types of cuprates by ARPES measurements, such as $La_{2-x}Sr_xCuO_4$ (LSCO) (25), $YBa_2Cu_3O_{6+\delta}$ (YBCO) (26), $(Bi,Pb)_2Sr_2CuO_{6+\delta}$ (Bi2201) (27), and $Bi_2Sr_2CaCu_2O_{8+\delta}$ (Bi2212) (28). Among them, LSCO is an ideal platform because the LT critical points (denoted as p_{FS}) in other cuprates are usually close to materials' doping solubility limit ($p_{FS} > 30\%$ in YBCO, $p_{FS} > 35\%$ in Bi2201, $p_{FS} > 29\%$ in Bi2212, but $p_{FS} < 22\%$ in LSCO). Nonetheless, the three-dimensionality of LSCO electronic structure broadens the critical point p_{FS} in two-dimensional cases to a finite doping range (29), within which electron-like and

Author contributions: Z.C. and Z.-X.S. designed research; Y.Z., Z.C., S.-D.C., K.-J.X., M.H., Y.H., D.L., and S.-K.M. performed research; Y.Z. analyzed data; M.H. and D. L. developed instruments for the experiment; S.-i.U. contributed samples; and Y.Z., Z.C., and Z.-X.S. wrote the paper.

Reviewers: P.A., Johns Hopkins University; and A.C., University of Bristol.

The authors declare no competing interest.

[1]Y.Z. and Z.C. contributed equally to this work.

[2]To whom correspondence may be addressed. Email: ylzhong@stanford.edu, zychen@stanford.edu, or zxshen@stanford.edu.

[3]Present address: Department of Physics, Southern University of Science and Technology, Shenzhen 518055, China.

This article contains supporting information online at http://www.pnas.org/lookup/suppl/doi:10.1073/pnas.2204630119/-/DCSupplemental.

Published August 1, 2022.

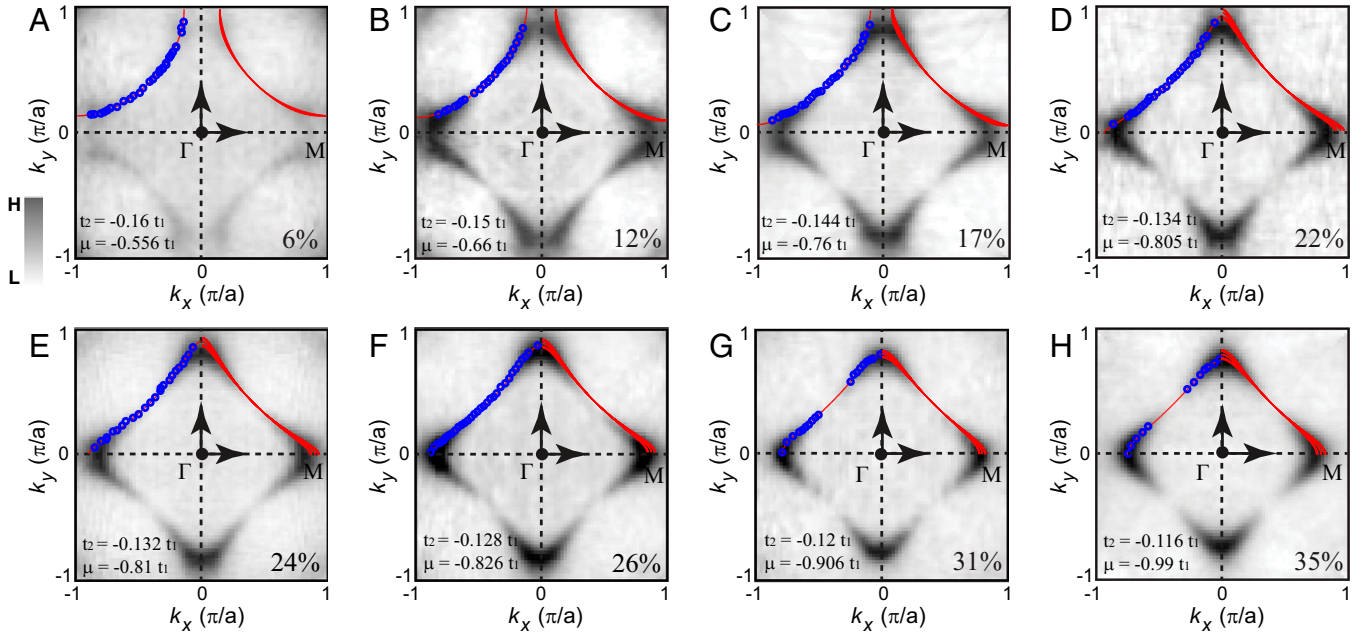

Fig. 1. Three-dimensional Fermi surface projected onto k_x–k_y plane. (*A*–*H*) Doping-dependent in-plane Fermi surface maps for $x = 0.06$ (*A*), 0.12 (*B*), 0.17 (*C*), 0.22 (*D*), 0.24 (*E*),0.26 (*F*), 0.31 (*G*), and 0.35 (*H*) samples. All the Fermi surfaces are integrated within the spectral weight window $E_F \pm 5$ meV ($x = 0.06$ sample with $E_F \pm 25$ meV due to the low intensity near E_F) and fourfold symmetrized in the first BZ. Fermi momentum k_F (blue circles) is determined by the peaks of the corresponding momentum distribution curves at E_F. Red curves in the top left quadrant of the BZ are simulating in-plane Fermi surfaces at $k_z = \pi/c$ ($h\nu = 70eV$). Red curves in the top right quadrant of the BZ are simulated three-dimensional Fermi surfaces projected onto k_x–k_y plane. We use $t_z = 0.03\ t_1$ for all simulations. Doping levels were determined by Luttinger theorem. Measurement temperature is 9 K. Details of band structure parameters t_1, t_2, t_3, and μ are listed in Table 1.

hole-like features coexist and manifest at different k_z. Therefore, a detailed doping-dependent and k_z-dependent photoemission study is needed to dissect the LT in LSCO.

Here we utilize a recently developed oxide molecular beam epitaxy system in situ connected to a synchrotron ARPES end station, for the synthesis of LSCO thin films with precise control of thickness and doping levels (*SI Appendix*, Fig. S1). Photon energy-dependent ARPES measurements with improved spectral quality (*SI Appendix*, Figs. S2 and S3) reveal an accurate out-of-plane hopping parameter, determining that the LT occurs within a certain doping range. This is close to the doping of the normal-state electronic specific heat divergence and rapid Hall number change (17–19). With the band parameters determined by fitting the electronic dispersions, we calculated the doping-dependent electronic specific heat and found a marked agreement with thermodynamic microcalorimetry experiment in the vicinity of LT (18), providing a band theory explanation for the specific heat peak, without the need for the additional contribution from quantum fluctuations at a putative critical point p^*. Furthermore, we perform a systematic angle-dependent gap measurement which shows persistent *d*-wave symmetry across the LT, with no enhancement of the gap magnitude near the VHS. Our findings are incompatible with existing scenarios of high-T_C superconductivity being associated with VHS (6, 7) and call for a critical reexamination of the evidence of quantum critical point in LSCO family of compounds.

Results

Three-dimensional Fermi surface can be probed with in-plane momentum $\mathbf{k}_{||}$ (a combination of k_x and k_y) and out-of-plane momentum k_z. In ARPES measurements, we access these momenta through the following relations:

$$|\mathbf{k}_{||}| = \sqrt{2m(h\nu - \phi - E_B)}\sin\theta/\hbar, \qquad [1]$$

$$k_z = \sqrt{2m[(h\nu - \phi - E_B)\cos^2\theta + V_0]}/\hbar, \qquad [2]$$

where m is the electron mass, ϕ is the sample work function, E_B is the binding energy, θ is the polar angle with respect to the surface normal, and V_0 is the inner potential. First, as displayed in Fig. 1, we focus on the in-plane Fermi surface evolution at a selected photon energy $h\nu = 70$ eV (the selection of this photon energy will be discussed below). According to the Luttinger theorem, we calculate the doping levels via counting the filled states enclosed by the Fermi surface contours. In the following discussion, all the doping levels are determined by this method (*SI Appendix*, Table S1 summarizes the information of samples). Second, we explore the out-of-plane Fermi surface by tuning the photon energies from 60 to 150 eV. A periodic k_F–k_z dispersion on the $x = 0.22$ sample is shown in Fig. 2*A* (see *SI Appendix*, Fig. S3 for more details). Inner potential $V_0 = 9$ eV is obtained by analyzing experimental data and considering the periodicity of Brillouin zones (BZ). To avoid the inconsistency from weaker spectral intensity around E_F at some photon energies, we choose momentum k_B (at binding energy $E_B = -20$ mV) as a fingerprint to quantify the k_z dispersion. A sinusoidal-like k_B–k_z relation is observed along the (0, 0) to (π, 0) direction on both $x = 0.22$ and 0.35 samples, in contrast to the negligible variation along the (0, 0) to (π, π) direction (Fig. 2*B*). We use a three-dimensional tight-binding model to simulate the Fermi surface (29),

$$\begin{aligned} E_{3D}(k_x, k_y, k_z) = &-\mu - 2t_1[\cos(k_x a) + \cos(k_y a)] \\ &-4t_2\cos(k_x a)\cos(k_y a) \\ &-2t_3[\cos(2k_x a) + \cos(2k_y a)] \\ &-2t_z\cos\left(\frac{k_x a}{2}\right)\cos\left(\frac{k_y a}{2}\right)\cos\left(\frac{k_z c}{2}\right) \\ &\times[\cos(k_x a) - \cos(k_y a)]^2. \end{aligned} \qquad [3]$$

Here t_1, t_2, and t_3 are the first, second, and third nearest neighbor hopping integrals between Cu sites. t_z represents the

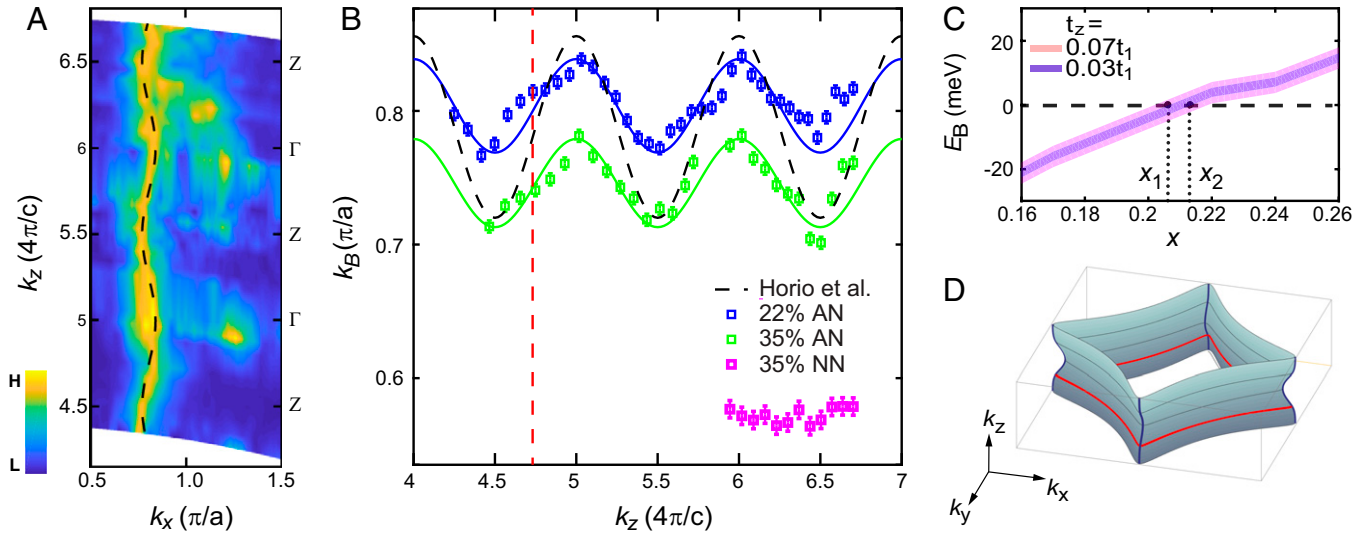

Fig. 2. Three-dimensional Fermi surface projected onto k_x–k_z plane. (*A*) Out-of-plane Fermi surface map along antinodal direction [from (0, 0) to (π, 0)] for $x = 0.22$ sample. Photon energies are swept in the range 60 to 150 eV to cut different k_z planes. (*B*) k_B–k_z dispersion along antinodal direction for $x = 0.22$, 0.35 sample (blue and green squares), and along nodal direction [from (0, 0) to (π, π)] for $x = 0.35$ sample (magenta squares). k_B is the momentum located at the energy contour $E = -20$ mV. Error bars denote the uncertainty to obtain k_B. The blue and green lines represent the three-dimensional tight-binding simulations. The black dashed line comes from ref. 16. Red dashed line is the corresponding k_z at photon energy $h\nu = 70$ eV. (*C*) Doping-dependent binding energy E_B at momentum $k = (0.98\,\pi, 0.02\,\pi)$. Results from two interlayer hopping parameters ($t_z = 0.03\ t_1$, $0.07\ t_1$) are shown. Smaller t_z narrows the LT regime into $x = 0.206$ to 0.214. Violet and pink areas represent the binding energy range for the two different values of k_z, respectively. x_1 and x_2 are the lower and upper bounds of the LT range. (*D*) Three-dimensional Fermi surface illustration of LSCO at $x = 0.22$. The red contour is the in-plane Fermi surface at $k_z = \pi/c$. Measurement temperature is 150 K.

interlayer hopping coefficient. μ is the chemical potential. a is the in-plane lattice constant. $c/2$ is the distance between adjacent CuO_2 layers. In particular, the $\cos(k_xa/2)\cos(k_ya/2)[\cos(k_xa) - \cos(k_ya)]^2$ term accounts for the staggered stacking of neighboring CuO_2 planes in the body-centered tetragonal structure of LSCO. Considering the universality of constant nodal Fermi velocity in a wide doping range of LSCO (30), we choose t_1 = 190 (±15) meV (determined by fitting the nodal dispersions from E_F to –30 meV on all measured samples) and $t_3/t_2 = -0.5$ for all samples and tune t_2, t_z, and μ to depict the topography change of the Fermi surface (Table 1 and *SI Appendix*, Fig. S4 summarize all the band parameters). The shift of μ is associated with the band filling effect from Sr dopants. The doping-dependent t_2 corresponds to a combined effect from chemical doping and electron correlation (31, 32) and evolves smoothly across the LT. t_z can be determined by fitting the experimental data via Eq. **3**: t_z = 0.030 (±0.004) t_1 on the $x = 0.22$ sample, and t_z = 0.039 (±0.005) t_1 on the $x = 0.35$ sample. $t_z = 0.03t_1$ is used to simulate the three-dimensional Fermi surfaces, as shown in the top right quadrant in each panel of Fig. 1. To quantify the LT regime accurately, we interpolate t_2 and μ linearly to obtain the doping-dependent antinode's binding energy. This provides an estimated range of LT from $x = 0.206$ to 0.214 (the error bar for x is 0.01), as shown in Fig. 2*C*. The three-dimensional Fermi surface for $x = 0.22$ is illustrated in Fig. 2*D*, where the red contour denotes the in-plane Fermi surface at $h\nu = 70$ eV. We selected this photon energy in Fig. 1 because the corresponding k_z ($\approx \pi/c$) locates at the midpoint between the largest and the smallest Fermi surfaces, making it the most representative for the study of LT and doping level characterization.

Having identified the LT in LSCO, we next examine its influence on the superconductivity. A typical Fermi surface map ($x = 0.22$) covering the first and second BZs is shown in Fig. 3*A*, in which we selected an antinodal cut in the first BZ and a nodal cut in the second BZ (for higher spectral intensity due to the matrix element effect in ARPES) as examples. The corresponding energy–momentum plots and energy distribution curves (EDC) are presented in Fig. 3 *B*–*E*. While no gap opening is found at the node (Fig. 3*C*), there is a noticeable intensity depletion around E_F for the antinode (Fig. 3*B*), implying an anisotropic gap structure. Quantitative analysis of gap symmetry in the superconducting state is shown in Fig. 4. As displayed in Fig. 4 *A*–*D*, we obtained the gap size by fitting the symmetrized EDC at k_F with respect to E_F, using formula $A(\omega) = -1/\pi\ \mathrm{Im}(1/(\omega - \Sigma(\omega)))$ with a constant background subtracted, where ω is the binding energy. The self-energy $\Sigma(\omega)$ term can be expressed as $\Sigma(\omega) = -i\Gamma + \Delta^2/\omega$, where Γ is the lifetime of quasiparticles, and Δ is the gap (33). Gaussian convolution representing the instrumental resolution was applied to the spectral functions. For overdoped films (x = 0.17, 0.22, and 0.24), the symmetrized EDC at antinode shows two coherence peaks with a gap opening. Moving from the antinode toward the node, the gap size decreases, and finally, a single peak forms at the node. Angle-dependent gap sizes are plotted in Fig. 4 *E*–*H*. Canonical *d*-wave pairing symmetry is observed across the LT (x = 0.17, 0.22, and 0.24). For x = 0.26 and higher dopings, the gap is below the detectable limit. On the underdoped side ($x = 0.12$), there is an obvious deviation of the antinodal gap from the *d*-wave extrapolation,

Table 1. Band structure parameters

x	t_1 (meV)	t_2/t_1	t_3/t_1	t_z/t_1	μ/t_1
6%	190	−0.16	0.08	0.03	−0.556
12%	190	−0.15	0.075	0.03	−0.66
17%	190	−0.144	0.072	0.03	−0.76
22%	190	−0.134	0.067	0.03	−0.805
24%	190	−0.132	0.066	0.03	−0.81
26%	190	−0.128	0.064	0.03	−0.826
31%	190	−0.12	0.06	0.03	−0.906
35%	190	−0.116	0.058	0.03	−0.99

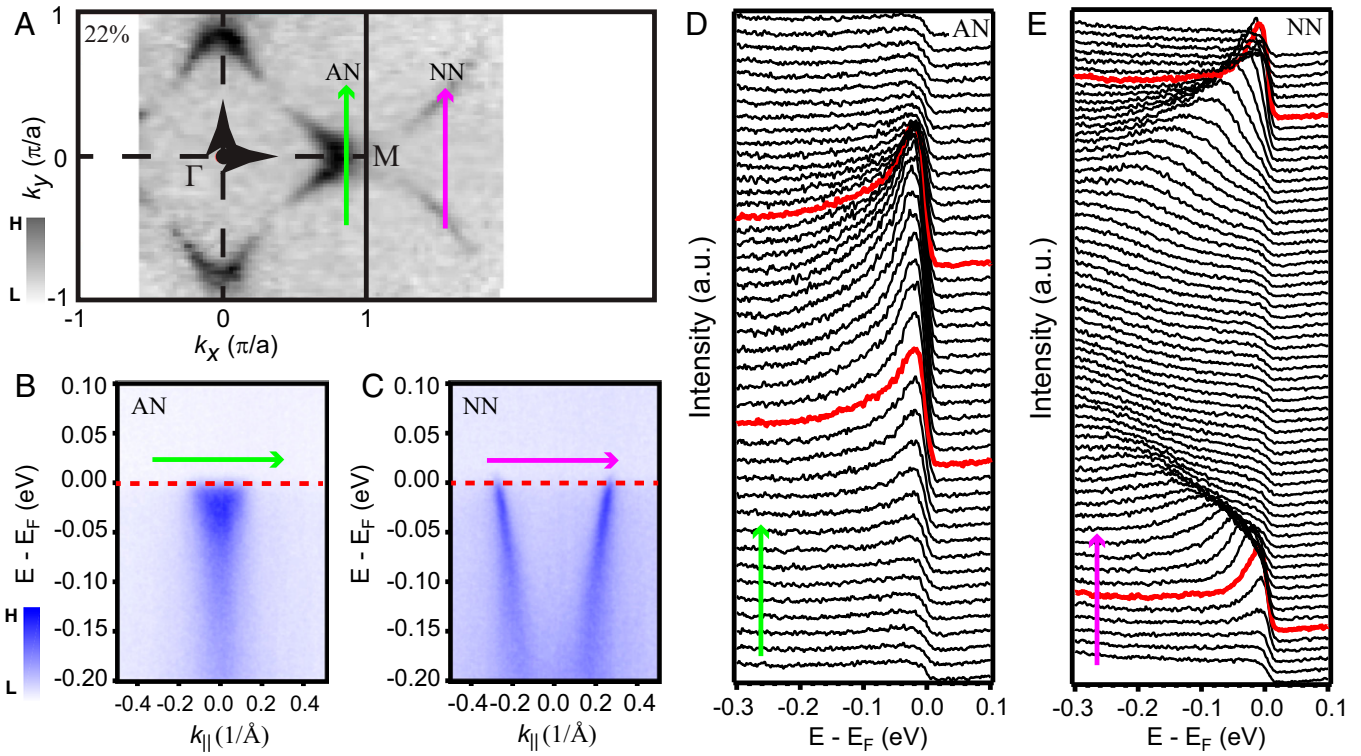

Fig. 3. Low-energy electronic structure of LSCO at $x = 0.22$. (*A*) In-plane Fermi surface map covering first and second BZs. Due to the matrix element effect, we measure antinodal spectra in the first BZ and nodal spectra at the second BZ. (*B* and *C*) Energy–momentum spectra along antinodal (green arrow) and nodal (magenta arrow) cuts. Red dashed line denotes the Fermi level. (*D* and *E*) The corresponding EDC curves along antinodal and nodal cuts labeled by green and magenta arrows, respectively. Red curves are the EDCs at Fermi momenta k_F values. k_F in *D* is determined by the minimum gap criterion. Measurement temperature is 9 K.

indicating the dominant influence of pseudogap in the antinodal regime. This node–antinode dichotomy is a generic feature in underdoped cuprates (34, 35).

Discussion

The established three-dimensionality of Fermi surface is crucial for understanding the specific heat anomaly in LSCO. Thermodynamic measurements of Nd-LSCO display a divergence of the normal-state electronic specific heat in the vicinity of LT (17), which was seen as a key signature to the existence of quantum critical point p^* inside the superconducting dome. Theoretically, electronic specific heat (usually referred to as Sommerfeld coefficient γ) is the temperature derivative of total quasiparticle entropy S (36),

$$S = k_B \int [-flnf - (1-f)\ln(1-f)]\rho(E)dE. \quad [4]$$

Here f is the Fermi–Dirac function, k_B is the Boltzmann constant, and $\rho(E)$ represents the density of state (DOS) at binding energy E. Given that γ is closely related to the DOS near E_F, we calculate the doping-dependent $\rho(E)$:

$$\rho(E) = (1/4\pi^3) \int d\mathbf{k}/\partial\varepsilon(\mathbf{k}), \quad [5]$$

where $d\mathbf{k}$ is the volume element in the momentum space. In the two-dimensional case, LT is associated with the divergence of DOS known as VHS, arising from the chemical potential crossing a saddle point at (π, 0), which also generates a significant anistropy of DOS along the Fermi surface (see *SI Appendix*, Fig. S5 for details). In the LSCO system, three-dimensionality reduces this divergence to a finite sharp peak. Below, we refer to this peak still as VHS for convenience.

In previous single-crystal studies of LSCO, Nd-LSCO, and Eu-LSCO, VHS was considered insufficient to account for the electronic specific heat maximum (16–18). In our analysis, we introduce doping-dependent t_2 and t_3 parameters extracted directly from ARPES spectra, incorporating electron correlation effect caused by chemical doping. Considering the updated band parameters and the smaller t_z we obtained, we revisit the relationship between VHS and the electronic specific heat by using Eq. **4**. In order to make a direct comparison between thin film and single crystal, we benchmark our thin film data by performing ARPES measurement on an $x = 0.22$ single-crystal sample under the identical experimental setup. We find the same Luttinger volume (=22%) and t_z (=0.032 ± 0.004 t_1) parameter as the results from $x = 0.22$ thin film within experimental errors (*SI Appendix*, Fig. S6).

Fig. 5*A* displays the calculated γ based on the extracted band parameters from ARPES data. We compare the ARPES-derived γ at 2 K with the data from thermodynamic measurements in LSCO and Zn-LSCO (18, 37, 38), revealing a marked consistency near the LT. Both the location (i.e., doping) and the magnitude of the specific heat peak agree between the ARPES derivation and thermodynamic measurements. The fact that such a simple approach captures the basic shape of the γ curve is striking. This indicates that the topological transition of the Fermi surface contributes dominantly to the specific heat peak in LSCO. Quantum critical fluctuations at p^*, if they exist, possibly only play a minor role for the magnitude of specific heat near the LT. Note that the ARPES measured band parameters (e.g., t_2) evolve smoothly across the LT (*SI Appendix*, Fig. S4), also indicating no sign of additional renormalization from quantum critical contributions. On the

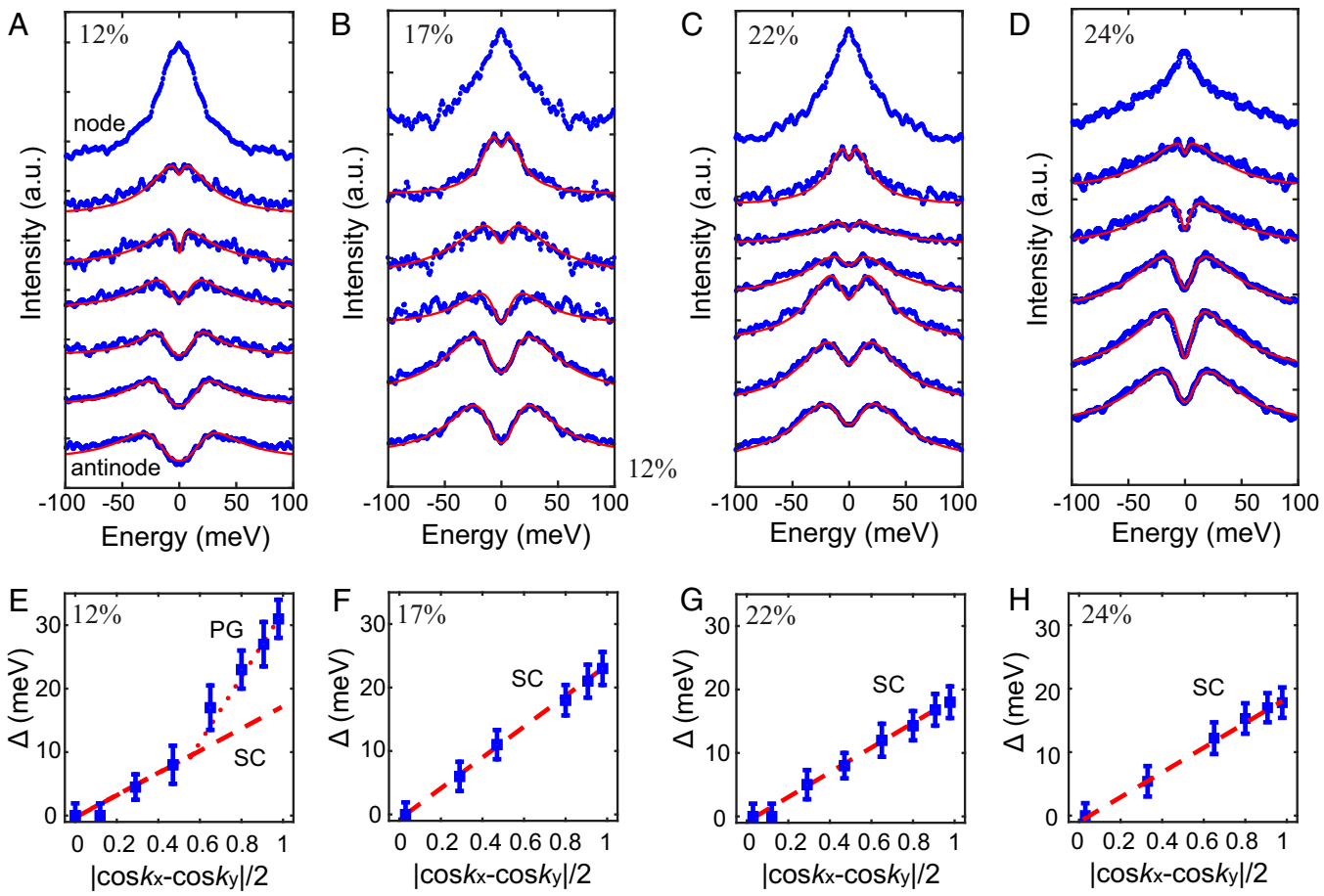

Fig. 4. Superconducting gap symmetry. (*A–D*) Angle-dependent symmetrized EDCs at k_F values for $x = 0.12$, 0.17, 0.22, and 0.24 samples. The red lines are fittings to obtain the gap sizes. (*E–H*) Angle-dependent gap sizes for $x = 0.12$, 0.17, 0.22, and 0.24 samples. Dashed red lines are guides for the *d*-wave pairing symmetry. Dotted red line denotes the dominant contribution of pseudogap around antinodal regime. Error bars reflect the fitting uncertainty in determining Δ. Measurement temperature is 9 K.

underdoped side (6 and 12%), doping-dependent Fermi arc length (39) is considered to calculate the γ values (DOS is counted only within the Fermi arc regime), which also agrees with the thermodynamic data. Yet, the ARPES derived γ in overdoped regime is roughly 30% smaller than the thermodynamic values. The temperature dependence of the $x = 0.22$ ARPES-derived γ (*SI Appendix*, Fig. S7) shows a saturation below 2 K, which may explain the consistency between 2 K thermodynamic data (18) and extrapolated 0 K thermodynamic data (37, 38) in LSCO. For Nd-LSCO and Eu-LSCO cases, additional γ increase below 2K might signify additional effects from quantum criticality at p^* (17), yet it is to be understood why the quantum critical point p^* stemming from other electronic orders [e.g., spin stripes peaking around 1/8 doping (40)] could coincide with the Fermi surface LT doping p_{FS}, unless such order makes the layers less coupled and thus more two-dimensional which enhances the DOSs at VHS. With more prominent γ divergence, Nd-LSCO and Eu-LSCO have lower T_C compared to LSCO, indicating a reversed correlation. We note that similar analysis between VHS and specific heat maximum has been reported in strontium ruthenates (41, 42), and elastocaloric contribution to the entropy has been identified (43).

Previous specific heat analysis usually includes strong disorder scattering effect based on transport measurement (16–18). Fig. 5*B* summarizes the specific heat simulations under several t_z parameters and scattering rate $\hbar/\tau$. However, the measured γ of Zn-LSCO has no significant difference compared with LSCO (37, 38) (also seen in Fig. 5), while disorder scattering of Zn-LSCO in transport measurements is apparently higher (44). This casts questions on whether disorder effect in transport and thermodynamic measurements are identical. In our analysis of the ARPES-derived γ, we adopt the assumption that the effect of transport disorder is negligible in thermodynamic measurements, based on the observations of similar measured γ values in LSCO with and without Zn substitutions (18, 37, 38).

Except for the divergent behavior of γ, there are other experimental observations pointing to a putative quantum critical point p^* in cuprates. One of them is the rapid Hall number change from p to $1 + p$ at the pseudogap endpoint in Nd-LSCO and YBCO (19, 45), perhaps corresponding to an LT across the critical point. However, transport experiments display no sign of p to $1 + p$ transition over a wide range of doping in LSCO (46–49) and Bi2201 (50), which implies that the sharp change of Hall effect at p^* is not a universal feature in cuprates. Furthermore, systematic doping-dependent ARPES antinodal data are not consistent with a second-order quantum phase transition (51).

Finally, we discuss the role of LT on superconductivity. Our results show that the VHS with significantly enhanced DOS has little effect on both the superconducting gap size and gap symmetry in LSCO system. In Bi2201 and Bi2212, the LT is found experimentally coinciding with the overdoped endpoint

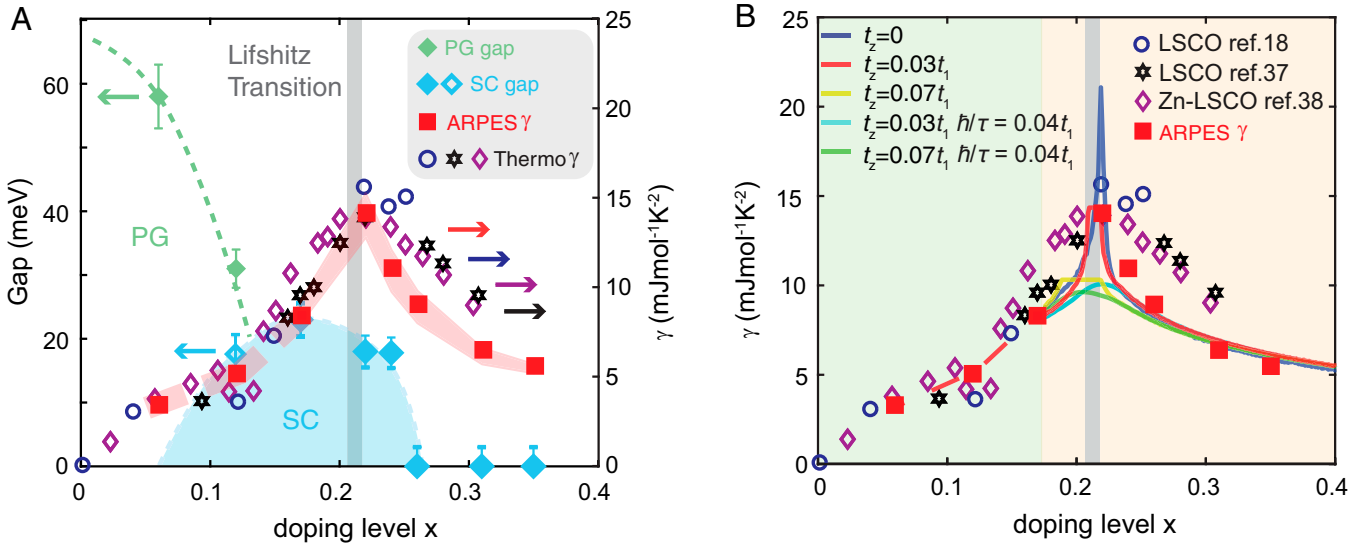

Fig. 5. Doping-dependent electronic specific heat and phase diagram of LSCO. (*A*) Phase diagram of LSCO. Blue solid diamonds are doping-dependent superconducting gaps. Blue open diamond corresponds to the extrapolated SC gap at $x = 0.12$ in Fig. 4*E*. Green diamonds correspond to the measured pseudogap in the underdoped regime. Error bars reflect the fitting uncertainty in determining the gaps. Gray vertical area represents the LT range, the same as the range between x_1 and x_2 in Fig. 2*C*. Red squares are electronic specific heat coefficients (γ) calculated at 2 K based on ARPES-derived band structure parameters (Fermi arc length is considered in the cases of $x = 0.06$ and 0.12). The shaded red curve represents the upper and lower bounds of the calculated γ by considering the uncertainty of t_1 (175 to 205 meV). $t_z = 0.03t_1$ is used here in the calculation. Also plotted are electronic specific heat coefficients (γ) obtained by thermodynamic measurements: blue open circles are from ref. 18 (measured at 2 K), black open stars are from ref. 37 (extrapolated to 0 K), and purple open diamonds are from ref. 38 (extrapolated to 0 K). (*B*) Calculated electronic specific heat coefficients (γ) under different interlayer hopping parameters t_z (0, 0.03 t_1 and 0.07t_1) and scattering rates $\hbar/\tau$ (0, 0.04t_1). $t_z = 0.07t_1$ is the hopping parameter used in ref. 16. $\hbar/\tau = 0.04t_1$ is the scattering rate used in ref. 17. The light yellow area indicates the regime in which we use underlying band structure to calculate specific heat coefficient γ. The light green area indicates the regime with Fermi arc consideration.

of superconductivity (27, 28). This correlation has been considered as a possible interpretation for the disappearance of superconductivity in overdoped cuprates. Dynamical cluster approximation calculation (10) displayed a spin susceptibility transition from antiferromagnetic type peaked at $q = (\pi, \pi)$ to ferromagnetic type centered at $q = (0, 0)$ across the critical point p_{FS}. In addition, renormalization group analysis (11) and quantum Monte Carlo simulation (52) both predicted the existence of ferromagnetic fluctuations at van Hove filling in two-dimensional Hubbard model, which has been observed recently in heavily overdoped *p*-type and *n*-type cuprates (53, 54). We have shown that LSCO system manifests robust *d*-wave superconductivity across the LT, and the transition point p_{FS} is far away from the SC endpoint, incompatible with the theoretical prediction of triplet *p*-wave pairing beyond the LT. An alternative theoretical proposal to the reduced superconductivity is that the flat band dispersion near antinode makes the *d*-wave pairing sensitive to impurity concentrations that increase with x (55–57).

In conclusion, by systematic ARPES measurements on LSCO thin films, we accurately determined the doping range where the LT occurs. Based on the similar γ values between LSCO and more disordered Zn-LSCO that excludes disorder effect in specific heat measurements, we adopt a simple band model and found a marked consistency between γ calculated from ARPES band parameters and that from thermodynamic measurements in the vicinity of LT. These results show that in the LSCO system, the proposed quantum criticality at p^* is not required to account for the magnitude of the electronic specific heat peak. We further unambiguously show that the superconducting gap maintains persistent *d*-wave symmetry with no obvious enhancement of magnitude on both sides of the LT. Our results reveal the differentiated roles of LT on thermodynamics and superconductivity in LSCO: the LT causes the thermodynamic specific heat peak but has almost no effect on superconducting gap size and symmetry.

Materials and Methods

$La_{2-x}Sr_xCuO_4$ thin films with $x = 0.06$, 0.12, 0.17, 0.22, 0.24, 0.26, 0.31, and 0.35 were synthesized on $LaSrAlO_4$ (001) substrates in a Veeco GEN930 MBE system with continuous supply of purified ozone. The growth process was monitored by in situ reflective high-energy electron diffraction. Metal sources are individually shuttered to realize layer-by-layer control of the growth, ensuring an atomically flat surface without impurities for optimized ARPES measurements. All samples presented in this work were 13.3 nm thick (10 unit cells) with LaO termination. The growth was performed at 700 °C, under background pressure of 1×10^{-5} Torr of purified ozone. After the growth, the sample was immediately transferred under ultrahigh vacuum to the ARPES end station at Stanford Synchrotron Radiation Lightsource beamline 5-2 equipped with a Scienta DA30 analyzer. The base pressure during the ARPES measurements was better than 3×10^{-11} Torr. Linear-horizontally polarized light with $h\nu = 70$ eV was used to map the Fermi surface and detect the gap structure. Measurement temperature was 9 K, and the corresponding energy resolution was 12 meV. The k_z dispersion was studied within a photon energy range 60 to 150 eV and temperature at 150 K. A previous $Sr_3Ru_2O_7$ study (41) that found a quantitative agreement between the quasiparticle DOS and the electronic specific heat inspired us to use band parameters to derive and compare with specific heat data in LSCO. We use fitted band parameters from the three-dimensional Fermi surface to calculate the Fermi velocity and the associated DOS as described in the Discussion since it is better constrained with lower error level than local extractions, especially for the antinode regime. More details about the growth and measurement are shown in *SI Appendix*.

Data Availability. Data presented in this manuscript are available in the Stanford Digital Repository at https://purl.stanford.edu/xm139vq7575 (58). All other study data are included in the article and/or *SI Appendix*.

ACKNOWLEDGMENTS. We thank S. A. Kivelson, D. H. Lee, T. P. Devereaux, D. J. Scalapino, P. J. Hirschfeld, and E. Huang for stimulating discussions. ARPES

experiments were performed at Beamline 5-2, Stanford Synchrotron Radiation Lightsource, Stanford Linear Accelerator Center (SLAC) National Accelerator Laboratory. This work was supported by the US Department of Energy (DOE), Office of Science, Office of Basic Energy Sciences, Materials Sciences and Engineering Division, under contract DE-AC02-76SF00515. The work at Advanced Light Source, Lawrence Berkeley National Laboratory, was supported by US DOE under contract DE-AC02-05CH11231.

Author affiliations: [a]Stanford Institute for Materials and Energy Sciences, Stanford Linear Accelerator Center (SLAC) National Accelerator Laboratory, Menlo Park, CA 94025; [b]Advanced Light Source, Lawrence Berkeley National Laboratory, Berkeley, CA 94720; [c]Geballe Laboratory for Advanced Materials, Stanford University, Stanford, CA 94305; [d]Department of Applied Physics, Stanford University, Stanford, CA 94305; [e]Stanford Synchrotron Radiation Lightsource, Stanford Linear Accelerator Center (SLAC) National Accelerator Laboratory, Menlo Park, CA 94025; [f]Department of Applied Physics, Yale University, New Haven, CT 06511; [g]Department of Physics, University of Tokyo, Tokyo 113-0033, Japan; and [h]Department of Physics, Stanford University, Stanford, CA 94305

1. B. Keimer, S. A. Kivelson, M. R. Norman, S. Uchida, J. Zaanen, From quantum matter to high-temperature superconductivity in copper oxides. *Nature* **518**, 179–186 (2015).
2. A. Damascelli, Z. Hussain, Z. X. Shen, Angle-resolved photoemission studies of the cuprate superconductors. *Rev. Mod. Phys.* **75**, 473 (2003).
3. T. Timusk, B. Statt, The pseudogap in high-temperature superconductors: An experimental survey. *Rep. Prog. Phys.* **62**, 61 (1999).
4. E. Fradkin, S. A. Kivelson, J. M. Tranquada, Colloquium: Theory of intertwined orders in high-temperature superconductors. *Rev. Mod. Phys.* **87**, 457 (2015).
5. W. E. Pickett, Electronic structure of the high-temperature oxide superconductors. *Rev. Mod. Phys.* **61**, 433 (1989).
6. R. S. Markiewicz, A survey of the van Hove scenario for high-T_C superconductivity. *J. Phys. Chem. Solids* **58**, 1179 (1997).
7. D. M. Newns, C. C. Tsuei, P. C. Pattnaik, Anomalous isotope effect and van Hove singularity in superconducting Cu oxides. *Phys. Rev. B* **52**, 13611 (1995).
8. Y. He *et al.*, Superconducting fluctuations in overdoped $Bi_2Sr_2CaCu_2O_{8+\delta}$. *Phys. Rev. X* **11**, 031068 (2020).
9. W. Wu *et al.*, Pseudogap and Fermi-surface topology in the two-dimensional Hubbard model. *Phys. Rev. X* **8**, 021048 (2018).
10. T. A. Maier, S. Karakuzu, D. J. Scalapino, Overdoped end of the cuprate phase diagram. *Phys. Rev. Res.* **2**, 033132 (2020).
11. C. Honerkamp, M. Salmhofer, Magnetic and superconducting instabilities of the Hubbard model at the van Hove filling. *Phys. Rev. Lett.* **87**, 187004 (2001).
12. N. Doiron-Leyraud *et al.*, Pseudogap phase of cuprate superconductors confined by Fermi surface topology. *Nat. Commun.* **8**, 2044 (2017).
13. C. Proust, L. Taillefer, The remarkable underlying ground states of cuprate superconductors. *Annu. Rev. Condens. Matter Phys.* **10**, 409 (2019).
14. I. Božović, X. He, J. Wu, A. T. Bollinger, Dependence of the critical temperature in overdoped copper oxides on superfluid density. *Nature* **536**, 309–311 (2016).
15. F. Mahmood, X. He, I. Božović, N. P. Armitage, Locating the missing superconducting electrons in the cuprate $La_{2-x}Sr_xCuO_4$. *Phys. Rev. Lett.* **122**, 027003 (2019).
16. M. Horio *et al.*, Three-dimensional Fermi surface of overdoped La-based cuprates. *Phys. Rev. Lett.* **121**, 077004 (2018).
17. B. Michon *et al.*, Thermodynamic signatures of quantum criticality in cuprate superconductors. *Nature* **567**, 218–222 (2019).
18. C. Girod *et al.*, Normal state specific heat in the cuprate superconductors $La_{2-x}Sr_xCuO_4$ and $Bi_2Sr_{2-x}La_xCuO_{6+\delta}$ near the critical point of the pesudogap phase. *Phys. Rev. B* **103**, 214506 (2021).
19. C. Collignon *et al.*, Fermi-surface transformation across the pseudogap critical point of the cuprate superconductor $La_{1.6-x}Nd_{0.4}Sr_xCuO_4$. *Phys. Rev. B* **95**, 224517 (2017).
20. J. A. Sobota, Y. He, Z. X. Shen, Angle-resolved photoemission studies on quantum materials. *Rev. Mod. Phys.* **93**, 025006 (2021).
21. M. Platé *et al.*, Fermi surface and quasiparticle excitations of overdoped $Tl_2Ba_2CuO_{6+\delta}$. *Phys. Rev. Lett.* **95**, 077001 (2005).
22. N. E. Hussey, M. Abdel-Jawad, A. Carrington, A. P. Mackenzie, L. Balicas, A coherent three-dimensional Fermi surface in a high-transition-temperature superconductor. *Nature* **425**, 814–817 (2003).
23. J. He *et al.*, Fermi surface reconstruction in electron-doped cuprates without antiferromagnetic long-range order. *Proc. Natl. Acad. Sci. U.S.A.* **116**, 3449–3453 (2019).
24. T. Helm *et al.*, Evolution of the Fermi surface of the electron-doped high-temperature superconductor $Nd_{(2-x)}Ce_{(x)}CuO_{(4)}$ revealed by Shubnikov-de Haas oscillations. *Phys. Rev. Lett.* **103**, 157002 (2009).
25. T. Yoshida *et al.*, Systematic doping evolution of the underlying Fermi surface of $La_{2-x}Sr_xCuO_4$. *Phys. Rev. B* **74**, 224510 (2006).
26. V. B. Zabolotnyy *et al.*, Momentum and temperature dependence of renormalization effects in high-temperature superconductor $YBa_2Cu_3O_{7-y}$. *Phys. Rev. B* **76**, 064519 (2007).
27. T. Kondo *et al.*, Hole-concentration dependence of band structure in $(Bi,Pb)_2Sr_2CuO_{6+\delta}$ determined by the angle-resolved photoemission spectroscopy. *J. Electron Spectrosc. Relat. Phenom.* **663**, 137 (2004).
28. I. K. Drozdov *et al.*, Phase diagram of $Bi_2Sr_2CaCu_2O_{8+\delta}$ revisited. *Nat. Commun.* **9**, 5210 (2018).
29. S. Sahrakorpi, M. Lindroos, R. S. Markiewicz, A. Bansil, Evolution of midgap states and residual three dimensionality in $La_{2-x}Sr_xCuO_4$. *Phys. Rev. Lett.* **95**, 157601 (2005).
30. X. J. Zhou *et al.*, High-temperature superconductors: Universal nodal Fermi velocity. *Nature* **423**, 398 (2003).
31. E. Pavarini, I. Dasgupta, T. Saha-Dasgupta, O. Jepsen, O. K. Andersen, Band-structure trend in hole-doped cuprates and correlation with T_{cmax}. *Phys. Rev. Lett.* **87**, 047003 (2001).
32. M. Civelli, M. Capone, S. S. Kancharla, O. Parcollet, G. Kotliar, Dynamical breakup of the fermi surface in a doped Mott insulator. *Phys. Rev. Lett.* **95**, 106402 (2005).
33. M. R. Norman, M. Randeria, H. Ding, J. C. Campuzano, Phenomenology of the low-energy spectral function in high-T_C superconductors. *Phys. Rev. B* **57**, R11093 (1998).
34. W. S. Lee *et al.*, Abrupt onset of a second energy gap at the superconducting transition of underdoped Bi2212. *Nature* **450**, 81–84 (2007).
35. T. Yoshida *et al.*, Universal versus material-dependent two-gap behaviors of the high-Tc cuprate superconductors: Angle-resolved photoemission study of $La_{2-x}Sr_xCuO_4$. *Phys. Rev. Lett.* **103**, 037004 (2009).
36. N. W. Ashcroft, N. D. Mermin, *Solid State Physics* (Harcourt Brace College Publishers, New York, 1976), pp. 53–54.
37. N. Momono, T. Matsuzaki, M. Oda, M. Ido, Superconducting condensation energy and pseudogap formation in $La_{2-x}Sr_xCuO_4$: New energy scale for superconductivity. *J. Phys. Soc. Jpn.* **71**, 2832 (2002).
38. N. Momono *et al.*, Low-temperature electronic specific heat of $La_{2-x}Sr_xCuO_4$ and $La_{2-x}Sr_xCu_{1-y}Zn_yO_4$: Evidence for a d wave superconductor. *Physica C* **233**, 395 (1994).
39. T. Yoshida *et al.*, Low-energy electronic structure of the high-*TC* cuprates $La_{2-x}Sr_xCuO_4$ studied by angle-resolved photoemission spectroscopy. *J. Phys. Condens. Matter* **19**, 125209 (2007).
40. Q. Ma *et al.*, Parallel spin stripes and their coexistence with superconducting ground states at optimal and high doping in $La_{1.6-x}Nd0.4Sr_xCuO_4$. *Phys. Rev. Res.* **3**, 023151 (2021).
41. A. Tamai *et al.*, Fermi surface and van Hove singularities in the itinerant Metamagnet Sr3Ru2O7. *Phys. Rev. Lett.* **101**, 026407 (2008).
42. C. H. Mousatov, E. Berg, S. A. Hartnoll, Theory of the strange metal $Sr_3Ru_2O_7$. *Proc. Natl. Acad. Sci. U.S.A.* **117**, 2852–2857 (2020).
43. Y. S. Li *et al.*, Elastocaloric determination of the phase diagram of Sr_2RuO_4. *Nature* **607**, 276–280 (2022).
44. Y. Fukuzumi, K. Mizuhashi, K. Takenaka, S. Uchida, Universal superconductor-insulator transition and T_c depression in Zn-substituted high-T_c cuprates in the underdoped regime. *Phys. Rev. Lett.* **76**, 684–687 (1996).
45. S. Badoux *et al.*, Change of carrier density at the pseudogap critical point of a cuprate superconductor. *Nature* **531**, 210–214 (2016).
46. H. Y. Hwang *et al.*, Scaling of the temperature dependent Hall effect in $La_{2-x}Sr_xCuO_4$. *Phys. Rev. Lett.* **72**, 2636–2639 (1994).
47. Y. Ando, Y. Kurita, S. Komiya, S. Ono, K. Segawa, Evolution of the Hall coefficient and the peculiar electronic structure of the cuprate superconductors. *Phys. Rev. Lett.* **92**, 197001 (2004).
48. W. J. Padilla *et al.*, Constant effective mass across the phase diagram of high-*TC* cuprates. *Phys. Rev. B* **72**, 060511(R) (2005).
49. I. Tsukada, S. Ono, Negative Hall coefficients of heavily overdoped $La_{2-x}Sr_xCuO_4$. *Phys. Rev. B* **74**, 134508 (2006).
50. C. Putzke *et al.*, Reduced Hall carrier density in the overdoped strange metal regime of cuprate superconductors. *Nat. Phys.* **17**, 826 (2021).
51. S. D. Chen *et al.*, Incoherent strange metal sharply bounded by a critical doping in Bi2212. *Science* **366**, 1099–1102 (2019).
52. R. Hlubina, S. Sorella, F. Guinea, Ferromagnetism in the two-dimensional t-t' Hubbard model at the van Hove density. *Phys. Rev. Lett.* **78**, 1343 (1997).
53. K. Kurashima *et al.*, Development of ferromagnetic fluctuations in heavily overdoped $(Bi, Pb)_2(Sr, La)_2CuO_{6+\delta}$ copper oxides. *Phys. Rev. Lett.* **121**, 057002 (2018).
54. T. Sarkar *et al.*, Ferromagnetic order beyond the superconducting dome in a cuprate superconductor. *Science* **368**, 532–534 (2020).
55. N. R. Lee-Hone, V. Mishra, D. M. Broun, P. J. Hirschfeld, Optical conductivity of overdoped cuprate superconductors: Application to LSCO. *Phys. Rev. B* **98**, 054506 (2018).
56. Z. X. Li, S. A. Kivelson, D. H. Lee, Superconductor-to-metal transition in overdoped cuprates. *npj Quantum Mater.* **6**, 36 (2021).
57. G. Kim *et al.*, Optical conductivity and superconductivity in highly overdoped $La_{2-x}Ca_xCuO_4$ thin films. *Proc. Natl. Acad. Sci. U.S.A.* **118**, e2106170118 (2021).
58. Y. Zhong *et al.*, Differentiated roles of Lifshitz transition on thermodynamics and superconductivity in $La_{2-x}Sr_xCuO_4$. Stanford Digital Repository. https://purl.stanford.edu/xm139vq7575. Deposited 20 July 2022.